AIAA JOURNAL
Vol. 52, No. 2, February 2014

Turbulence Generation from a Sweeping-Based Stochastic Model

Anthony Lafitte*
Liebherr-Aerospace, 31016 Toulouse, France
Thomas Le Garrec†
ONERA–The French Aerospace Lab, F-92322 Châtillon, France
Christophe Bailly‡
École Centrale Lyon, 69134 Ecully, France
and
Estelle Laurendeau§
Liebherr-Aerospace, 31016 Toulouse, France

DOI: 10.2514/1.J052368

Stochastic methods are widely used because they constitute a low-cost computational-fluid-dynamics approach to synthesize a turbulent velocity field from time-averaged variables of a flowfield. A new combined stochastic method based on the sweeping hypothesis is introduced in this paper. This phenomenon, stating that inertial range structures are advected by the energy containing eddies, is known to be an important mechanism of the turbulent velocity field decorrelation process. The proposed method presents the advantage of being easily implementable and applicable to any three-dimensional configuration as long as a steady Reynolds-averaged Navier–Stokes computation of the flow is available and assuming that the considered turbulence physics is compatible with the hypotheses made to build the current numerical model. The developed method is applied on a subsonic round cold free jet. The validation study shows that the synthesized turbulent velocity fields reproduce statistical features of the flow, such as two-point two-time velocity correlation functions, comparable to those found experimentally and integrates shear effects of the mean flow. The mean convection velocity of the turbulent structures is also correctly modeled. In addition, the turbulent kinetic energy spatial distribution is preserved by the stochastic method.

Nomenclature

A_n	=	amplitude of the nth mode
C_K	=	Kolmogorov constant
D	=	nozzle diameter
$D_{1/2}$	=	half-velocity diameter
E	=	von Kármán-Pao energy spectrum
k	=	wave number
k_c	=	cutoff wave number
k_e	=	wave number for which the maximum of energy occurs
$k_{\min}$	=	minimum wave number
$k_{\max}$	=	maximum wave number
k_n	=	wave number of the nth mode
k_t	=	turbulent kinetic energy
$k_{t\,\max}$	=	maximum turbulent kinetic energy
L	=	integral length scale
L_η	=	Kolmogorov length scale
N	=	number of modes
R_{ij}	=	velocity correlation function
$\boldsymbol{r}$	=	$\sqrt{\xi_j^2}$, separation vector
t	=	time
$\boldsymbol{u}$	=	total turbulent velocity field
$\bar{\boldsymbol{u}}$	=	mean flow velocity field
$\boldsymbol{u}_a$	=	mean velocity on the jet axis $\boldsymbol{u}(x, y = 0, z)$
$\boldsymbol{u}_{\text{bulk}}$	=	carrier vector field
$\boldsymbol{u}_c$	=	convection velocity
$\boldsymbol{u}_l$	=	large-scale turbulent velocity field
$\boldsymbol{u}_s$	=	small-scale turbulent velocity field
$\boldsymbol{u}_j$	=	jet exit velocity
x, y, z	=	positions
x_i	=	positions
α_L	=	length calibration factor
α_τ	=	time calibration factor
δ	=	boundary-layer thickness
δ_θ	=	momentum thickness
ε	=	dissipation rate
ζ	=	random velocity field
ν	=	kinematic viscosity
ξ_i	=	separation in the ith direction
σ_n	=	direction of the nth mode
τ	=	time delay
τ_c	=	time scale
φ_n	=	phase of the nth mode
ω_n	=	pulsation of the nth mode

Subscripts

l	=	large scale
n	=	mode number
s	=	small scale

Presented as Paper 2011-2888 at the 17th AIAA/CEAS Aeroacoustic Conference, Portland, OR, 5–8 June 2011; received 3 October 2012; revision received 25 July 2013; accepted for publication 3 August 2013; published online 24 January 2014.

*Ph.D. Student, Research and Expertise Department; anthony.lafitte@liebherr.com.

†Research Engineer, Computational Fluid Dynamics and Aeroacoustics Department; thomas.le_garrec@onera.fr.

‡Professor; christophe.bailly@ec-lyon.fr. Senior Member AIAA.

§Research Engineer, Research and Expertise Department; estelle.laurendeau@liebherr.com.

I. Introduction

SINCE the beginning of the 1970s, the understanding of turbulent flows is a topic of the highest importance for actors of the aeronautic industry working on energy efficient or quiet designs for aircraft. As a result of the significant advancement in computational capabilities over the last decades, many numerical tools allowing the simulation of turbulent flows have been developed. In most of the computational fluid dynamics (CFD), the turbulence modeling is needed and constitutes a key issue of the simulations. For instance, one can quote the Reynolds stresses models used in the framework of steady Reynolds-averaged Navier–Stokes (RANS) computations or the variety of subgrid-scale models developed for large-eddy simulation (LES) applications.

Numerous studies in fields of application as diverse as particle diffusion [1–5], turbulence injection at the inlet boundary of unsteady calculations [6–9], or aeroacoustics [10–15] leaned upon stochastic methods to model the turbulence. This kind of approach presents the advantage of being easily applicable and less expensive than direct computations. The challenge imposed by those methodologies is to synthesize an unsteady turbulent velocity field with "realistic" features starting from time-averaged information about a given flowfield. Interested in particle diffusion in incompressible, stationary, and isotropic turbulence, Kraichnan [1] was the first to propose a method to generate a stochastic velocity field $\boldsymbol{u}$ by considering a sum of Fourier modes. The methods proposed since his former model [1] to compute such fields can be separated into two families: those based on the decomposition in turbulent modes, and those leaning upon the filtering of a white noise.

The first family of models have been widely applied [13,15–20] in the framework of aeroacoustics studies. The idea is to build the stochastic velocity field as a sum of N modes whose amplitudes are directly dictated by an imposed energy spectrum. Following the work of Karweit et al. [10] on the propagation of an acoustic wave through a turbulent medium, Bechara et al. [11] proposed an approach by generating N_r pairwise independent realizations of the stochastic field constituted of N spatial Fourier modes and considerating it as a time series. With each local velocity signal being random, the temporal coherence of the turbulence is then recovered by a filtering of each local white noise in the frequency domain by a Gaussian function centered on a characteristic frequency ε/k_t. Bailly et al. [21] and later Bailly and Juvé [12] decided to take into account the temporal evolution of $\boldsymbol{u}$ directly in the turbulence generation process. In practical terms, they added a time-evolving term to Kraichnan's formulation [1] involving a convection velocity $\boldsymbol{u}_c$ and a pulsation ω_n to generate unfrozen turbulence. The main issue of such an improvement is that both $\boldsymbol{u}_c$ and ω_n have to be spatially constant to avoid a total decorrelation of the velocity field at large times [22]. However, the turbulent fields generated by these methods [11,12,21] reproduce the proper spatial characteristics, but their temporal evolution is poorly modeled. To remedy the problem, Billson et al. [14,23,24] considered locally that the turbulent field was a superposition of a white noise and an advected term that is neither more nor less the turbulent field at the previous time step convected by the mean flow velocity. This method allows a good modeling of the space and time statistical features of the turbulence and is able to deal with inhomogeneous flowfield [18]. Nevertheless, the preservation of the local turbulent kinetic energy, which is by construction the base of a Fourier modes method, is lost because the turbulent velocity field $\boldsymbol{u}$ partly depends on upstream point conditions. Later, they also included an anisotropy model proposed initially by Smirnov et al. [25].

As well, approaches in Fourier modes are still widely used to study particle diffusion [2–5,26] in turbulent media. One can quote the development of the kinematic simulation (KS), which is very similar to Kraichnan's method [1]. In particular, Fung et al. [2] proposed an alternative version to the KS initial formulation by considering the sweeping hypothesis, or the fact that the small-scale vortices are advected by the energy containing eddies. They introduced a separation between large and small-scale velocity fields, with the latter part being advected by the first one.

Turbulent modes-based formulations are used as well to impose isotropic synthetic fluctuations as inlet boundary conditions for unsteady simulations [9,27]. One can quote the work of Lee et al. [6], who built a fluctuating signal by an inverse Fourier transform of randomly phased Fourier coefficients preliminary computed from a given two-dimensional (2-D) spectrum $E(k_1, k_2)$ or the frozen turbulence generation method proposed by Na and Moin [28].

Another way to compute a turbulent velocity field is by filtering, which can be spatial or temporal, of a white noise. In the case of spatial filtering, the filter kernel is built with either the targeted space–time correlation functions or an imposed energy spectrum. Many formulations have been proposed to improve the former works of Careta et al. [29], who generated a stochastic field from a random stream function. The random particle mesh (RPM) method developed by Ewert and Edmunds [30], followed by Ewert [13], has been applied to investigate slat [31] and jet [32] noise. In RPM, the streamlines are discretized regarding the time step and the local mean velocity of the flow. At each time step, the random particles, carrying the local stream function, located at each point of this grid are convected to the next point downstream before the advected random field is filtered. The resulting stream function mapping is then interpolated on the Computational AeroAcoustics grid, and the turbulent velocity field is obtained locally by the rotational of the stream function. More recently, Ewert [13] significantly reduced the computation cost of RPM by reducing the number of injected particles (fast RPM). Siefert and Ewert [32] and later Ewert et al. [33] also studied the sweeping effect and its influence on sound generation in jets.

The filtering of the white noise can also be achieved in the time domain. Initially frozen, the behavior of the turbulence carried by the mean flow in the RPM method is now driven by a Langevin equation [31,34,35], which is massively used to describe turbulence temporal evolution [34,36,37]. Working with a Langevin equation, random particles carrying the stream function are placed along the streamlines according to the time step and the mean flow. In this case, the algorithm can be seen as series of convection and decorrelation steps. The convection is modeled in the same manner as for the RPM method, and the decorrelation process is achieved by applying a Langevin equation. Numerical problems can arise when the latter equations are used, source terms for the Acoustic Perturbation Equations or Euler equations coming from time derivatives of a filtered white noise may be quite discontinuous, so that a second-order Langevin model sometimes needs to be considered to overcome this numerical issue [32,37]. The approaches by filtering present the advantage of being capable to reproduce perfectly the second-order two-point correlation tensor of homogeneous isotropic turbulence. Nevertheless, these approaches are still difficult to apply to the study of three-dimensional (3-D) complex geometries in spite of the recent development of a 3-D modal stochastic source model designed for an axisymmetric jet [38,39].

As for the Fourier modes formulations, the filtering-based approaches also constitute a useful tool in the field of unsteady computations initialization [27]. One can quote the contribution of Klein et al. [7] or the development of the SEM method by Jarrin et al. [8,40].

Pointing out the facts that, on one hand, methods relying on Fourier modes cannot model properly both convection and temporal evolution of the turbulence, and on the other hand, that filtering approaches are not suitable to study 3-D complex configurations, an innovative stochastic model inspired by the previous presented works is introduced in this paper. Developed initially for confined subsonic jet applications, the main constraint is to take the sweeping hypothesis into account. This phenomenon, stating that inertial range structures are advected by the energy containing eddies, is identified as an important mechanism of the decorrelation process of the turbulent velocity field [2,41–43]. This approach should be able to reproduce statistical properties of turbulence, such as velocity correlation functions, and to preserve the spatial distribution of the turbulent kinetic energy (TKE) imposed by the steady RANS simulation inputs. This methodology presents the advantage of being easily implementable and less expensive in CPU hours than direct computations. It should be applicable to any 3-D complex configurations as long as a steady computation of the flow is available to feed the model and the considered turbulence physics is compatible with the hypotheses made to build the current numerical model. This sweeping-based stochastic model and its parametrization are presented in Sec. II. Section III is devoted to a validation study concerning aerodynamics of a single subsonic cold free jet at Mach 0.72. Computations have been performed on 2-D grids by considering only the longitudinal and radial components of the velocity field. The velocity field generator has then been applied to a full 3-D subsonic jet configuration, and a discussion about the turbulent kinetic energy preservation is developed in Sec. IV.

II. Turbulence Generation Process

A stochastic method ensuring the generation of a turbulence satisfying some requirements is introduced in this section.

A. Overview of the Model

The method presented in this work allows the generation of stochastic turbulent velocity fields. The synthesization process of these unsteady fields is based on the sweeping hypothesis because this phenomenon is known to play a crucial role in the decorrelation process of the unsteady velocity field [2,41–43]. A separation in the turbulence scales is thus required. Following the former idea of Fung et al. [2], the turbulent velocity field $\boldsymbol{u}$ is split into two parts, respectively linked to the large and small-scale structures:

$$\boldsymbol{u}(\boldsymbol{x}, t) = \boldsymbol{u}_l(\boldsymbol{x}, t) + \boldsymbol{u}_s(\boldsymbol{x}, t) \tag{1}$$

The field $\boldsymbol{u}_l$ is provided by the Bailly and Juvé [12] method deriving straightforwardly from the former model of Kraichnan [1], while the field $\boldsymbol{u}_s$ is obtained from an adaptation of the Billson et al. [14] approach. The starting point to compute $\boldsymbol{u}_l$ and $\boldsymbol{u}_s$ is the local definition of an energy spectrum. Following the homogeneous isotropic turbulence hypothesis, a von Kármán–Pao spectrum is imposed at each grid point depending on the local transport variables k_t and ε:

$$E(k) = \alpha_E(\varepsilon L_e)^{2/3}(kL_e)^{-5/3} f_L(kL_e) f_\eta(kL_\eta) L_e \tag{2}$$

where L_e, corresponding approximately to the wave number k_e to whom the maximum of energy occurs [44], is related to the local integral length scale L by the relation $L_e \simeq L/0.747$; with L being defined by

$$L = \alpha_L(2/3k_t)^{3/2}\varepsilon^{-1} \tag{3}$$

and $L_\eta = (\nu^3/\varepsilon)^{1/4}$ designates the Kolmogorov length scale linked to the smallest turbulent motions in the flow. The choice of the calibration factor α_L in Eq. (3) has always been a topic of discussion and particularly in the field of aeroacoustics, where this coefficient is determined by calibrating the model directly on the far-field acoustic spectra. However, the setup of α_L will be discussed in the Sec. III.C. In Eq. (2), f_L and f_η are specified nondimensional functions. The function f_L drives the shape of the energy-containing part of the spectrum, while f_η represents its dissipation range. The specifications of f_L and f_η are

$$\begin{cases} f_L(kL_e) = \left(\frac{kL_e}{\sqrt{1+(kL_e)^2}}\right)^{17/3} \\ f_\eta(kL_\eta) = \exp[-2(kL_\eta)^2] \end{cases} \tag{4}$$

The function f_L defined in relation (4) tends to unity for $kL_e \gg 1$ and varies proportionally to $(kL_e)^4$ when $kL_e \ll 1$. Conversely, the definition of f_η in relation (4) leads to $f_\eta \to 0$ for $kL_\eta \ll 1$. In the inertial subrange, the Kolmogorov $-5/3$ spectrum is recovered. In Eq. (2), the constant α_E is set to the value $1.2/\alpha_L^{-2/3}$. The von Kármán–Pao energy spectrum is plotted in Fig. 1 for a given doublet (k_t, ε).

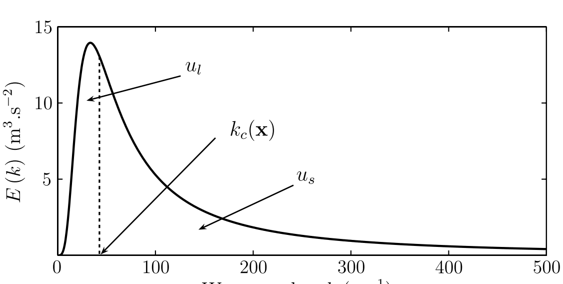

Fig. 1 Contribution of u_l and u_s in a generic von Kármán–Pao spectrum.

As shown in Fig. 1, the separation between large and small scales is achieved by introducing a cutoff wave number k_c. Because the sweeping hypothesis corresponds to the advection of the inertial range turbulent structures by the energy-containing eddies [32], k_c is chosen locally to fall just after the spectrum maximum:

$$k_c = 1.8 \qquad k_e = \frac{1.8}{L_e} \tag{5}$$

The energy spectrum is discretized using N modes of wave number k_n linearly distributed between a minimum wave number $k_{\min}$ and a maximum wave number $k_{\max}$. One can remark that logarithmic distributions providing a better discretization of the spectrum E in the lower wave number range have been tested as well in [11,12], but numerical results showed no major differences. In the case of inhomogeneous flowfield, k_c varies spatially so that the numbers of modes respectively linked to the large-scale structures N_l and small-scale structures $N_s = N - N_l$ vary spatially as well. However, the same wave-number range $[k_{\min}, k_{\max}]$ is used for the whole computational domain.

1. *Computation of the Large-Scale Velocity Field* $\boldsymbol{u}_l$

Following the expression proposed by Bailly and Juvé [12], the velocity field $\boldsymbol{u}_l$ associated to the large-scale eddies is decomposed as a sum of N_l Fourier modes:

$$\boldsymbol{u}_l(\boldsymbol{x}, t) = 2\sum_{n=1}^{N_l} \mathrm{A}_n \cos(\boldsymbol{k}_n(\boldsymbol{x} - \boldsymbol{u}_c t) + \omega_n t + \varphi_n)\sigma_n \tag{6}$$

with amplitude $A_n = \sqrt{E(k_n)\Delta k_n}$ built from the von Kármán–Pao energy spectrum, which depends on the local steady RANS variables. $\boldsymbol{k}_n$ and φ_n are the wave vector and the phase of the nth mode, respectively. $\boldsymbol{k}_n$ is defined by the coordinates (k_n, ϕ_n, θ_n) as shown in Fig. 2. The incompressibility hypothesis imposes $\boldsymbol{k}_n \cdot \boldsymbol{\sigma}_n = 0$; $\boldsymbol{\sigma}_n$ is therefore perpendicular to $\boldsymbol{k}_n$ and exclusively defined by the angle α_n.

The isotropic nature of the modeled turbulence requires to pick $\boldsymbol{k}_n$ randomly on a sphere of radius $\|\boldsymbol{k}_n\| = k_n$. The probability density functions for the parameters ϕ_n, θ_n, and α_n are defined in Table 1. The homogeneity hypothesis imposed to the flowfield leads to pick φ_n randomly between $[0; 2\pi]$.

In Eq. (6), the convection velocity $\boldsymbol{u}_c$ and the pulsation ω_n need imperatively to be constants in space to avoid a decorrelation of the generated velocity field at large times [22]. With $\boldsymbol{u}_l$ being defined locally, $\boldsymbol{u}_c$ allows the modeling of the turbulent structure's displacement downstream of the flow. For instance, for subsonic jet application, $\boldsymbol{u}_c$ might be set to $0.6\boldsymbol{u}_j$ in accordance with experiments [45], where $\boldsymbol{u}_j$ designates the jet exit velocity. ω_n stands for the temporal pulsation of the nth mode. The Kolmogorov pulsation defined by Eq. (7) is chosen for ω_n because it is the most appropriate choice for low wave numbers [3], and it gives more accurate results than, for instance, the Heisenberg pulsation [44,46]. To avoid spatial variations of ω_n, which could lead to unwanted decorrelation process, a mean value of the dissipation rate $< \varepsilon >$ is used to calculate ω_n,

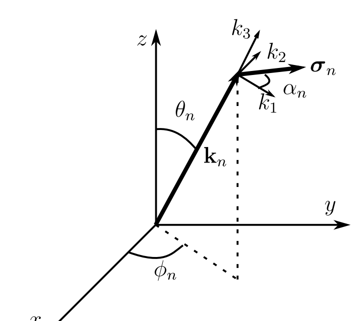

Fig. 2 Wave vector geometry for the nth Fourier velocity mode.

Table 1 Density probability functions of the stochastic parameters

Variables	Probability functions	Interval
ϕ_n	$P(\phi_n) = 1/(2\pi)$	$0 \le \phi_n \le 2\pi$
φ_n	$P(\varphi_n) = 1/(2\pi)$	$0 \le \varphi_n \le 2\pi$
α_n	$P(\alpha_n) = 1/(2\pi)$	$0 \le \alpha_n \le 2\pi$
θ_n	$P(\theta_n) = (1/2)\sin(\theta_n)$	$0 \le \theta_n \le \pi$

where $< . >$ designates the average over the most energetic points (i.e., all the points where k_t is greater than a prescribed threshold value $k_{\text{threshold}}$):

$$\omega_n = C_k^{1/2} < \varepsilon >^{1/3} k_n^{2/3} \tag{7}$$

The term $\boldsymbol{u}_l$ can therefore be explicitely formed at each time step of the numerical simulation. One can note that, by construction, $\boldsymbol{u}_l$ preserves the turbulent kinetic energy locally imposed to the large-scale structures:

$$\frac{1}{2} \overline{u_{l_i} u_{l_i}} = \sum_{n=1}^{N_l} A_n^2 = \sum_{n=1}^{N_l} E(k)\Delta k \approx \int_{k_{\min}}^{k_c} E(k)\,\mathrm{d}k \tag{8}$$

2. Computation of the Small-Scale Velocity Field $\boldsymbol{u}_s$

Fung et al. [2] wrote the temporal evolution of the small-scale structures velocity field $\boldsymbol{u}_s$ as resulting from the association of advection and decorrelation processes. They wrote, for a medium at rest,

$$\frac{\partial \boldsymbol{u}_s}{\partial t} = \underbrace{-\boldsymbol{u}_l \cdot \nabla \boldsymbol{u}_s}_{\text{advection}} \underbrace{-[(\boldsymbol{u}_s \cdot \nabla)\boldsymbol{u}_l + (\boldsymbol{u}_l \cdot \nabla)\boldsymbol{u}_s + 1/\rho \nabla p]}_{\text{decorrelation}} \tag{9}$$

In Eq. (9), p cannot be explicitly modeled so that Fung et al. [2] neglected the decorrelation term. In the present work, the building of the velocity field $\boldsymbol{u}_s$ linked to the small-scale vortices can also be seen as an association of advection and decorrelation processes. At a given temporal iteration m, the small-scale velocity field $\boldsymbol{u}_s^m$ is computed using a modified Billson et al. approach [14]. In other terms, the small-scale velocity field is defined by the following temporal filter

$$\boldsymbol{u}_s^m(\boldsymbol{x}) = a(\boldsymbol{x})\boldsymbol{u}_s^{m-1/2}(\boldsymbol{x}) + b(\boldsymbol{x})\zeta(\boldsymbol{x}) \tag{10}$$

In Eq. (10), $\boldsymbol{u}_s^m$ is written as a sum of an advected contribution $a(\boldsymbol{x})\boldsymbol{u}_s^{m-1/2}(\boldsymbol{x})$ and a random contribution $b(\boldsymbol{x})\zeta(\boldsymbol{x})$ that holds the decorrelation process. Unlike the works of Billson et al. [14,23] who resolve an advection equation with the conservative variables for $\boldsymbol{u}_s^{m-1/2}$, the advected term is here considered to be the small-scale velocity field at the previous time step $\boldsymbol{u}_s^{m-1}$, which is advected by the vector field $(\boldsymbol{u}_{\text{bulk}} + \boldsymbol{u}_l)$, with $\boldsymbol{u}_{\text{bulk}}$ being a carrier velocity vector field. In other words, $\boldsymbol{u}_s^{m-1/2}$ is obtained from $\boldsymbol{u}_s^{m-1}$ by solving the advection equation [Eq. (11)] that ensures the modeling of the sweeping effect:

$$\boldsymbol{u}_s^{m-1} \Rightarrow \frac{\partial \boldsymbol{u}_s}{\partial t} + (\boldsymbol{u}_{\text{bulk}} + \boldsymbol{u}_l^{m-1}) \cdot \nabla \boldsymbol{u}_s = \boldsymbol{0} \Rightarrow \boldsymbol{u}_s^{m-1/2} \tag{11}$$

One can note that, in the Fung et al. [2] study, $\boldsymbol{u}_s$ was simply advected by the field $\boldsymbol{u}_l$ because of a zero mean velocity field. In Eq. (10), the random term ζ is obtained as a sum of N_s spatial Fourier modes:

$$\zeta(\boldsymbol{x}) = 2 \sum_{n=N_l+1}^{N} \mathrm{A}_n \cos(\boldsymbol{k}_n \cdot \boldsymbol{x} + \varphi_n)\sigma_n \tag{12}$$

where the setup of the stochastic parameters A_n, $\boldsymbol{k}_n$, φ_n, and $\boldsymbol{\sigma}_n$ is achieved the same way than for $\boldsymbol{u}_l$, except that they are regenerated at each iteration. Consequently, ζ is a signal uncorrelated in space and time with a zero statistical mean value in time. In other terms, ζ is a locally white noise. This term therefore ensures the progressive decorrelation of $\boldsymbol{u}_s$. In Eq. (10), the definition of $a = e^{-\Delta t/\tau_c}$ guarantees the exponential decorrelation of the velocity field according to a characteristic time scale $\tau_c = \alpha_\tau k_t/\varepsilon$, with α_τ being a calibration factor. Finally, the coefficient $b = \sqrt{1-a^2}$ allows the conservation of the turbulent kinetic energy in homogeneous flows.

One should note that the present methodology does not include an explicit model for anisotropy. Few recent studies [17,18] showed that adding or not adding an anisotropy model to a Billson stochastic model had almost no influence on numerical results. Nevertheless, the advection equation [Eq. (11)] solved to compute the evolution of u_s introduces some anisotropy in the turbulent velocity field due to the mean flow inhomogeneity.

B. Description of the Algorithm Numerical Implementation

The initialization of the computation is achieved by calculating $\boldsymbol{u}_l(x, t_0)$ and imposing $\boldsymbol{u}_s(x, t_0) = \zeta(x, t_0)$. For a detailed explanation of the manner the algorithm works, one resumes the different steps of the method. At each iteration:

1) The field $\boldsymbol{u}_l$ is the first to be generated from Eq. (6).
2) Once done, the velocity field $\boldsymbol{u}_s^{t-\Delta t}$ linked to the small-scale structures at the previous time step is advected by the vector field $(\boldsymbol{u}_{\text{bulk}} + \boldsymbol{u}_l^{t-\Delta t})$ to obtain $\boldsymbol{v}$ from Eq. (11).
3) The white noise ζ is generated from Eq. (12).
4) The term $\boldsymbol{u}_s$ is computed, and finally, the turbulent velocity field $\boldsymbol{u}$ is formed using Eq. (1).
5) $\boldsymbol{u}_l$ and $\boldsymbol{u}_s$ are then stored to solve the advection equation [Eq. (11)] at the next time step.

III. Reproduction of the Space–Time Velocity Correlation Functions

The model presented in Sec. II is now evaluated in a free subsonic jet configuration. Aerodynamic statistical quantities of the flow such as two-point two-time velocity correlation functions R_{ij} defined by

$$R_{ij}(\boldsymbol{x}, \boldsymbol{r}, \tau) = \frac{\overline{u_i(\boldsymbol{x}, t)u_j(\boldsymbol{x}+\boldsymbol{r}, t+\tau)}}{\sqrt{\overline{u_i(\boldsymbol{x}, t)^2}}\sqrt{\overline{u_j(\boldsymbol{x}+\boldsymbol{r}, t+\tau)^2}}} \tag{13}$$

are computed. The studied jet is a cold subsonic jet at Mach 0.72, corresponding to a jet exit velocity of $u_j = 250\ \mathrm{m \cdot s^{-1}}$ with a nozzle diameter $D = 80$ mm. Numerical results are compared to experimental data obtained by Fleury et al. [45] for free jets at Mach 0.6 and 0.9.

A. Reynolds-Averaged Navier–Stokes Simulation

Mean flow and transport variables of the flowfield are provided by a RANS solution using the standard k_t-ε turbulence model. Many results concerning this jet configuration are available at ONERA, including experiments conducted in CEPRA 19 (ONERA's open-circuit anechoic wind tunnel, which is located in Saclay, France), LES calculations [47], or stochastic methods [15,17,19,48,49]. The first step of the study is to validate the RANS mean flow because it will serve as input data for the stochastic model. Some of the results obtained by Fleury et al. [45] are reminded concerning the half-velocity diameter and the momentum thickness. The respective evolutions of the half-velocity diameter $D_{1/2}$ and the momentum thickness δ_θ along the jet axis are depicted in Figs. 3a and 3b. RANS solution shows a good agreement with experimental data obtained by Fleury et al. [45].

Radial profiles of the axial mean velocity $\bar{u}$ for various longitudinal positions are shown in Fig. 4. The data collapse well with the classical hyperbolic tangent profile in the shear layer defined by

$$\frac{u}{u_a} = 0.5\left(1 - \tanh\left[\frac{D}{8\delta_\theta}\left(\frac{2y}{D} - \frac{D}{2y}\right)\right]\right) \tag{14}$$

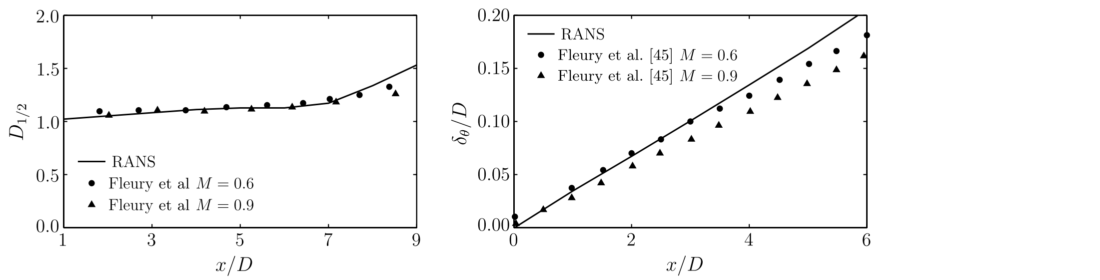

a) b)

Fig. 3 Representations of a) evolution of the half velocity diameter $D_{1/2}$ along the x direction, and b) evolution of the momentum thickness δ_θ along the jet axis.

B. Computational Setup

A validation study concerning the two-point two-time velocity correlation functions R_{ij} in the shear layer is conducted on 2-D grids, and results are compared to PIV measurements in the same planes. In this section, only the longitudinal and radial components of the velocity field are computed from the 3-D von Kármán–Pao spectra. Numerical results are shown for two points located at the center of the shear layer ($y = 0.5D$), as shown in Fig. 5. For the point P_1, a 161×61 points regular Cartesian grid is used with $\Delta x = \Delta y = 1$ mm. According to the acoustic dispersion relation $k = \omega/c$, this spatial resolution allows a $k_{\max}$ of 1000 m^{-1} so that k_n wave numbers are picked between 1 and 1000 m^{-1}. For the point P_2, a 181×81 point grid is used with $\Delta x = \Delta y = 2$ mm and $1 < k_n < 500$ m^{-1}. The chosen values of $k_{\max}$ allow the discretization of 75% of the turbulent kinetic energy provided by the RANS computation at the point P_1 and more than 85% of k_t at the point P_2. The time step Δt is set to 2.10^{-6} s for P_1 against 4.10^{-6} s for P_2. In both cases, 100 modes are used to discretize the von Kármán–Pao spectra. This choice allows a sufficient randomness of the velocity field while preserving a low computation time [44,46]. A simulation consists of 30,000 temporal iterations and is performed in a few minutes on an NEC SX8+ supercomputer. An averaging between 10 simulations is done to increase the statistics. The mean velocity $\bar{\boldsymbol{u}}$ is taken for the carrier velocity vector field $\boldsymbol{u}_{\text{bulk}}$ in Eq. (11) because it allows to include in the modeling the mean flow effects on the turbulence. The coefficient α_τ is set to 1 according to the literature [14,18]. Equation (11) is solved using the low-storage second-order optimized Runge–Kutta of Bogey and Bailly [50] with six under-stages and an 11-point fourth-order optimized Dispersive Relation Preserving scheme. An 11-point fourth-order spatial filtering is applied as well. Tam and Dong's [51] radiation boundary condition is set at the inlet of the computational domain, while outflow boundary conditions are imposed at the outlets.

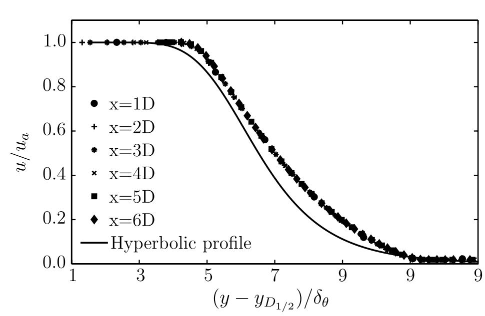

Fig. 4 Radial profiles of the axial mean velocity $\bar{u}$ for various longitudinal positions compared to the similarity law given in Eq. (14).

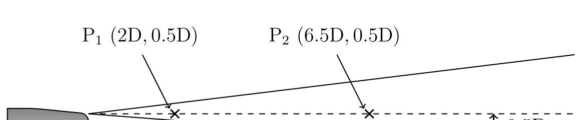

Fig. 5 Location of the two points studied in the present work.

C. Space Scales

In this section, the focus is on the purely spatial correlation functions $R_{ij}(\boldsymbol{x}, \boldsymbol{r}, 0)$ to check the coherence lengths of the synthesized turbulent velocity field.

1. *Calibration Factor* α_L

As mentioned before, the choice of the calibration factor α_L in Eq. (3) is a key point. In the field of free-jet aeroacoustics, many values can be found for α_L in the literature [14,17,18]. For instance, $\alpha_L = (2/3)^{3/2} = 0.544$ has been used by Billson et al. [14] or Dembinska [18] against $\alpha_L = 0.13$ by Omais et al. [17]. When used for acoustics applications, stochastic methods generally lead to an overestimation of the far-field acoustic spectra [11,12,14,18]. Decreasing α_L has the direct consequence to shift down the far-field spectra so that it has been used as an adjustment variable for those spectra levels.

This influence of α_L was expected because α_L governs k_e and therefore the energy distribution among the Fourier modes. The von Kármán–Pao spectrum at a given mesh point is shown in Fig. 6 for various values of α_L. For a constant $k_{\max}$, the calibration factor drives the amount of turbulent kinetic energy injected in the simulation and the definition of the most energetic modes.

Nevertheless, there should be a physical value for α_L depending on the configuration of interest. Experimentally, Fleury et al. [45] found that, for subsonic jets, the longitudinal integral length scale L_{11}^1 in the shear layer is nearly equal to $2\delta_\theta$, with δ_{theta} the momentum thickness. Approximating the momentum thickness δ_θ from the RANS computation by the relation

$$\delta_\theta = \int_0^\infty \frac{u}{u_a}\left(1 - \frac{u}{u_a}\right) \mathrm{d}r \tag{15}$$

The ratio between $2\delta_\theta$ and $(2/3k_t)^{3/2}/\varepsilon$ provides an estimate of the value of α_L. This quantity is plotted along the center of the shear layer in Fig. 7 and is found to be nearly equal to 1. Consequently, α_L is set to 1 in the present work.

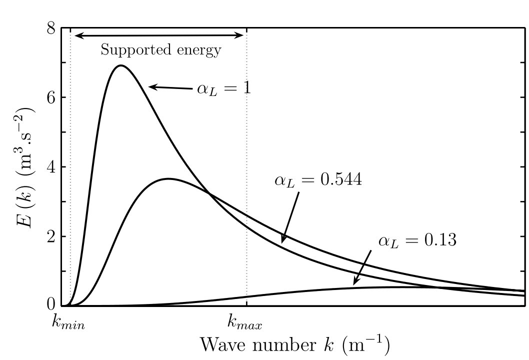

Fig. 6 Influence of the calibration factor α_L on the von Kármán–Pao spectrum.

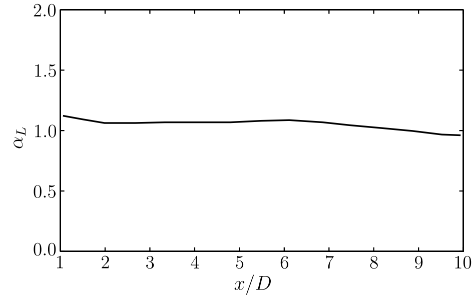

Fig. 7 Evolution of the ratio $(2\delta_\theta)/[(2/3k_t)^{3/2}/\varepsilon]$ along the axis $y = 0.5D$.

2. Numerical Results

The spatial correlation coefficient $R_{ii}(x, r, 0)$ is investigated at the point P_1. Correlation functions isocontours are depicted in Fig. 8 and compared to those measured by Fleury et al. [45]. The size and stretching of R_{11} and R_{22} patterns are modeled in a satisfying way. Nevertheless, the nonisotropic turbulence in the jet, which is not taken into account in this model, could explain some of the discrepancies between numerical and experimental results and the slight gap between R_{11} and R_{22} curves. The inclination of the isocontours of R_{11}, highlighted by Fleury et al. [45] and reported to be a mean flow effect, is recovered. The principal direction of R_{11} is approximately $\Theta = 19$ deg from the axial direction against $\Theta = 18$ deg in the literature [45]. Numerical errors arise at the entrance of the domain on both R_{11} and R_{22} isocontour patterns because of the influence of the inlet boundary condition because the extent of the computational domain is small and no turbulent structure is imposed at its inlet. The behavior of $R_{ii}(x, r, 0)$ along the line $y = 0.5D$ is plotted in Fig. 9a. A good agreement is found with experimental results obtained by Fleury et al. [45] at $M = 0.9$. One can note that R_{11} and R_{22} reach zero for points distant from P_1. Repeating this operation at different locations along the $y = 0.5D$ axis between $x = 2D$ and $x = 10D$, the longitudinal integral length scale $L_{11}^{(j)}$ along the jth direction from R_{11} can be computed at each longitudinal position by Eq. (16):

$$L_{11}^{(j)} = \frac{1}{2}\int_{-\infty}^{+\infty} R_{11}(x, x_j, 0)\,\mathrm{d}x_j \tag{16}$$

The longitudinal integral length scales $L_{11}^{(1)}$ along the center of the shear layer are depicted in Fig. 9b. Even if $L_{11}^{(1)}$ are overestimated by about 25%, the linear growth of $L_{11}^{(1)}$ along the $y = 0.5D$ axis is correctly simulated. Note that these results corroborate the setup of $\alpha_L = 1$.

D. Time Scales

The space–time velocity correlation functions $R_{ij}(x, r, \tau)$ are now studied at the point P_2. $R_{ii}(x, r, \tau)$ patterns are plotted for different values of the time delay τ in Fig. 10. The attenuation of $R_{ii}(x, r, \tau)$ is clearly visible as τ increases. The displacement of the correlation patterns according to the time delay τ is similar to those found in the experiments [45]. This is illustrated in Fig. 11, where present work results match the experimental curve. The location of the maximum of $R_{11}(x, r, \tau)$ according to the time delay τ along the center of the

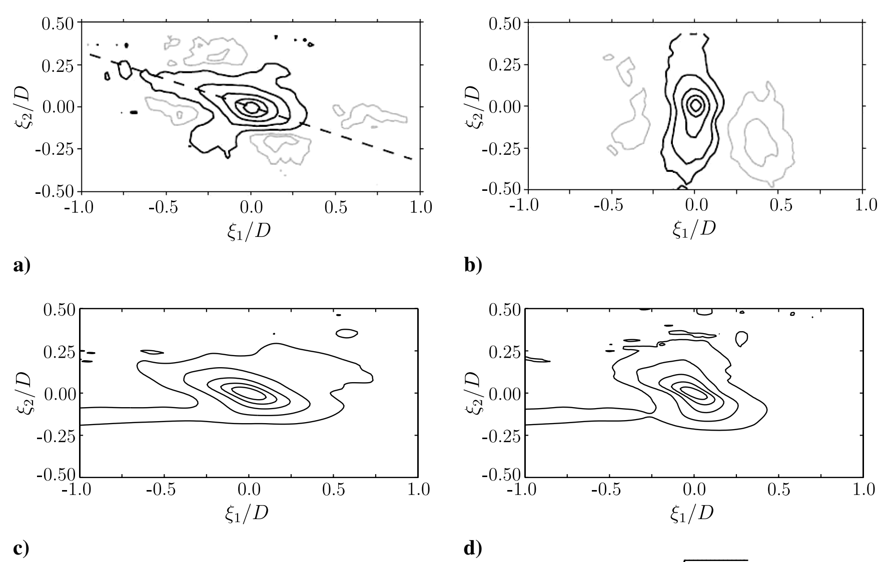

Fig. 8 Isocontours of $R_{11}(x,r,0)$ (Figs. 8a and 8c) and $R_{22}(x,r,0)$ (Figs. 8b and 8d). The distance $r = \sqrt{\xi_1^2 + \xi_2^2}$. R_{11} levels are (0.05, 0.2, 0.4, 0.6, 0.8), and R_{22} levels are (0.1, 0.2, 0.4, 0.6, 0.8). Experiments led by Fleury et al. [45] (top) and present work (bottom).

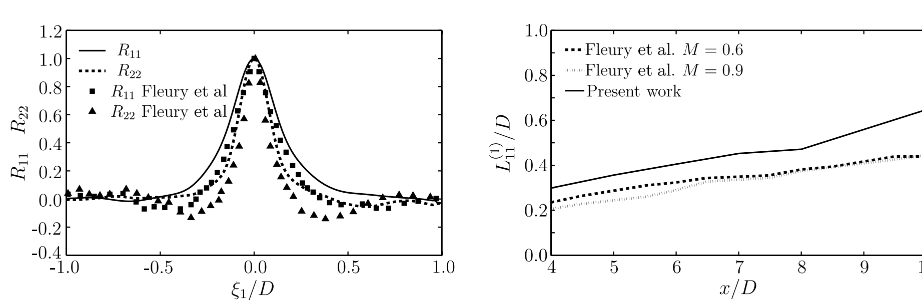

Fig. 9 Representations of a) evolution of $R_{ii}(x,r,0)$ along the center of the shear layer (the reference point is P_1), and b) evolution of the nondimensionalized longitudinal integral length scale $L_{11}^{(1)}/D$ along the center of the shear layer.

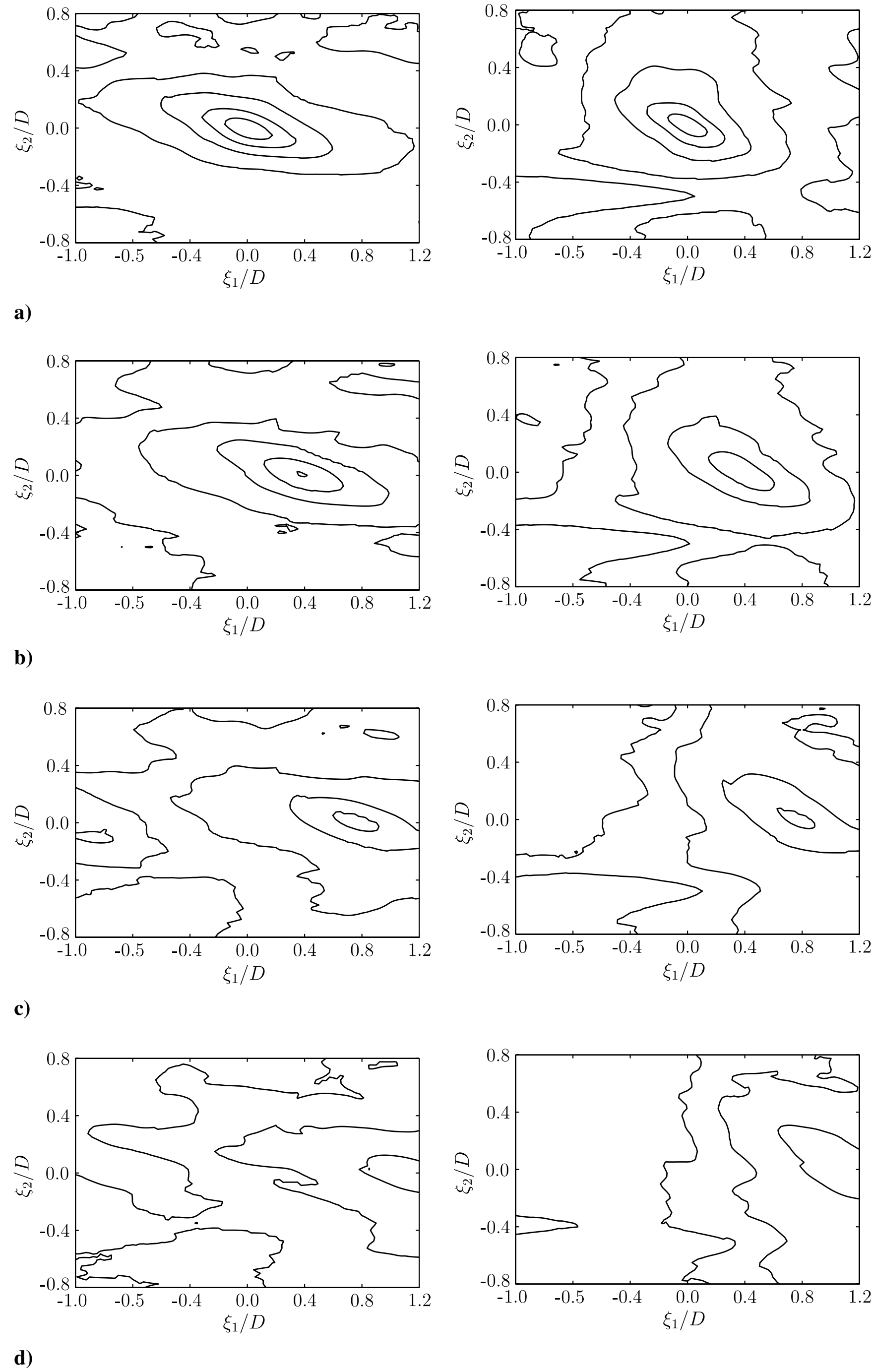

Fig. 10 On the left: $R_{11}(x,r,\tau)$ patterns. On the right: $R_{22}(x,r,\tau)$ patterns. The reference point is P_2. a) $\tau = 0$ μs, b) $\tau = 50$ μs, c) $\tau = 150$ μs, and d) $\tau = 245$ μs. Isocontour levels are (0.05, 0.2, 0.4, 0.6, 0.8).

shear layer is well reproduced. Furthermore, the slope of the curve in Fig. 11, corresponding to the mean convection velocity of the structures, is correctly modeled and equal to $0.6u_a$, with u_a being the velocity on the jet axis. The stochastic model developed in the present work therefore takes correctly into account the modeling of the turbulent structures in the shear layer. The decorrelation of the velocity field is studied at the point P_2 as well. The attenuation of the correlation functions R_{11} and R_{22} in the center of the shear layer is first investigated in an Eulerian frame in Fig. 12a. These curves show that R_{11} and R_{22} follow the same decorrelation law close to the R_{11} attenuation experimental function. Experiments [45] reveal more discrepancies between R_{11} and R_{22} decorrelation processes. In particular, the R_{22} attenuation curve decreases faster than the R_{11} one. This phenomenon is not reproduced by this approach. The attenuation of the correlation functions in a Lagrangian frame moving at the

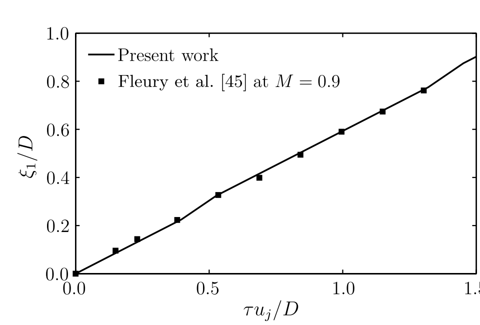

Fig. 11 Separation corresponding to the maximum of $R_{11}(x,r,\tau)$ in the convected frame according to the time delay τ. The reference point is P2.

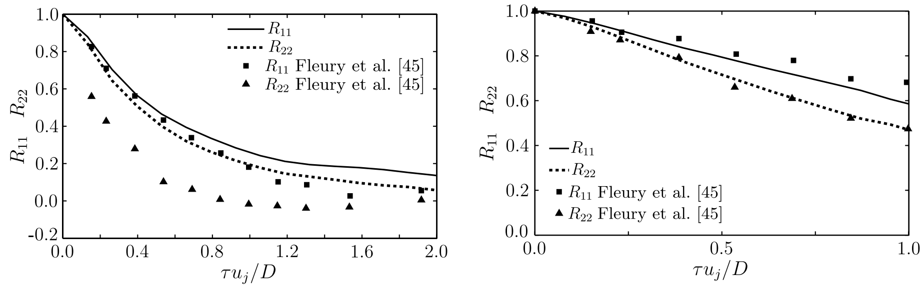

a) b)

Fig. 12 Representations of a) Eulerian decorrelation of the velocity field at the point P_2, and b) Lagrangian decorrelation of the velocity field. The reference point is P_2.

velocity u_c, i.e., $R_{ii}(x, u_c\tau, \tau)$ as a function of τ, is shown in Fig. 12b. Results are in good agreement with experimental data [45]. Using the present stochastic model, the decorrelation process of the turbulent velocity field is described more precisely in the Lagrangian frame. This is not a surprising result because Eq. (10) can be seen as a Langevin equation written in a Lagrangian frame. Such an equation states that, for a variable U along a streamline,

$$\frac{\partial}{\partial t}U = -\frac{1}{\tau}U + \sqrt{\frac{2}{\tau}}\zeta \tag{17}$$

When Eq. (17) is solved numerically [31,37], it shows similarities with Eq. (10). Indeed, one has

$$U(t+\Delta t) = \underbrace{\left(1-\frac{\Delta t}{\tau}\right)}_{\text{FE of } e^{-\Delta t/\tau}}U(t) + \underbrace{\sqrt{\frac{2\Delta t}{\tau}}}_{\text{FE of } \sqrt{1-e^{-2\Delta t/\tau}}}\zeta \tag{18}$$

where FE designates the first-order finite expansion of the given functions around the value 0, i.e., when $\tau \gg \Delta t$.

IV. Application to a Full Subsonic Jet

The sweeping-based stochastic model developed in Sec. III is able to synthesize a turbulent velocity field. In the case of a subsonic jet, it especially allows the reproduction of the velocity correlation functions in the shear layer, includes effect of the mean flow on the turbulence, and deals correctly with the convection velocity of the turbulent structures. Nevertheless, the validation study has been achieved by taking only the longitudinal and radial components of the unsteady velocity field and computing 2-D calculations on restricted grids. Full 3-D unsteady fields might be needed for certain applications such as aeroacoustics. Computing 3-D configurations implies a coarser resolution of the grid, and consequently a decreased $k_{\max}$, to keep a competitive computation time. In this section, the methodology has been evaluated on a 3-D computation including the whole jet plume. In addition, a discussion on the turbulent kinetic energy preservation is led.

A. Computational Setup

A 3-D cartesian grid consisting of $519 \times 108 \times 108$ mesh points has been generated. It extends up to $43D$ in the x direction and is bounded between $-5.5D$ and $5.5D$ in the y and z directions. In the vicinity of the nozzle exit, $\Delta x = \Delta y = \Delta z = \Delta = 5$ mm, leading to the ratio $\Delta/D = 0.0625$. This spatial resolution is held up to $28D$ in the x direction. According to the acoustic dispersion relation, this grid is therefore able to support a $k_{\max}$ up to 200 m^{-1}, leading to $k_{\max}D = 16$, which is a good compromise between the CPU cost and the quality of the aerodynamics modeling in the jet plume (see Sec. IV.B). Nevertheless, one can assume that this spatial resolution will lead to a poor discretization of the von Kármán–Pao spectra in the vicinity of the nozzle exit because $k_{\max}$ has been reduced by a factor of 5 from 1000 m^{-1} to 200 m^{-1} in comparison with the study led at the point P_1. The time step Δt is set to 8.10^{-6} s, and 100 modes are used to discretize the von Kármán–Pao spectra. A sponge zone is set up from $x = 20D$ to the exit of the computational domain to avoid the creation of spurious reflections that could contaminate the numerical solution when turbulent structures cross the exit boundary condition. According to the literature [44,46], a k_{treshold} equal to one-third of the maximum kinetic energy observed in the computation domain $k_{t\,\max}$ is taken. A resulting averaged dissipation rate of $<\varepsilon>= 278,000$ m$^2\cdot$s^{-3} is then used to compute the ω_n. One can notice that simulations have also been achieved by changing the parameter $k_{\text{threshold}}$ from $k_{t\,\max}/5$ to $k_{t\,\max}/2$, but results showed no significant differences. Numerical results have been obtained from a single simulation consisting of 20,000 temporal iterations, which has been achieved in 7 h on an NEC SX8+ supercomputer.

B. Reproduction of the Space–Time Velocity Correlation Functions

It is essential to check that the results obtained in Sec. III are not to highly affected computing 3-D simulations with a lower $k_{\max}$. During the 3-D computation, a 2-D grid comparable in size to the one used in Sec. III at the point P_2 has been extracted to compute space–time velocity correlation functions. $R_{ii}(x, r, 0)$ isocontours are plotted in Fig. 13. The sizes and inclination of the correlation patterns are preserved in comparison with Fig. 10a.

The displacement of the maximum of $R_{11}(x, r, \tau)$ is plotted versus the time delay τ in Fig. 14. The diminution of the resolution has a clear impact on the modeling of the convection velocity of the

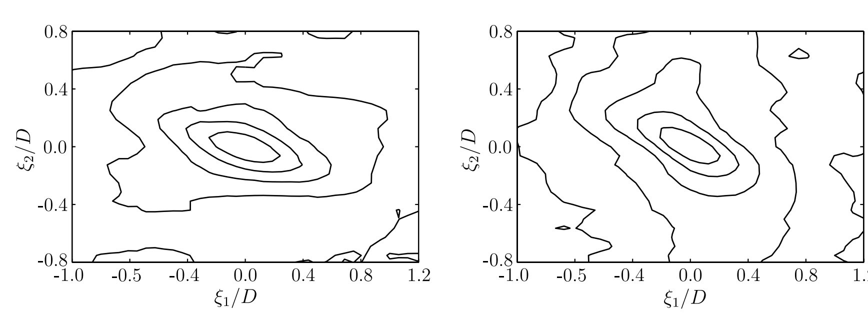

a) b)

Fig. 13 The reference point is P_2: a) $R_{11}(x,r,0)$ correlation patterns, and b) $R_{22}(x,r,0)$ correlation patterns. Isocontour levels are (0.05, 0.2, 0.4, 0.6, 0.8).

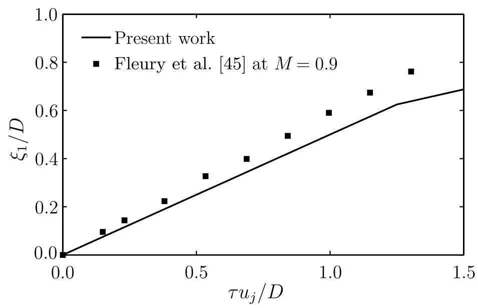

Fig. 14 Separation corresponding to the maximum of $R_{11}(x,r,\tau)$ in the convected frame according to the time delay τ. The reference point is P_2.

structures in the shear layer, passing from $0.6u_j$ to approximately $0.52u_j$. The decorrelation of the synthesized velocity field in an Eulerian and a Lagrangian frame is shown in Fig. 15. Results are slightly altered as well by the change in the parameterization, but the decorrelation process is not destructed, with results being in good agreement with those of [45]. The use of a coarser mesh than the 2-D one may be responsible for the observed discrepancies in comparison with the results provided by the 2-D study. The grid size has been increased from 2 to 5 mm at point P_2, and the corresponding range of wave numbers is reduced by the same ratio 2.5. To show the impact of a decreased maximum wave number, 2-D simulations have been performed at points P_1 and P_2 (as explained in Sec. III.B by changing the modeled $k_{\max}$). Figure 16 shows the modeling of $L_{ii}^{(j)}$, the directional integral length scale (longitudinal or radial) in the jth direction, as a function of the chosen maximum wave number. Ten simulations with a constant $\Delta k = 5\ \mathrm{m}^{-1}$ have been averaged to compute $L_{ii}^{(j)}$. The curves on Figs. 16a and 16b both show that maximum wave numbers set in Sec. III at points P_1 and P_2 allow a reasonable modeling of $L_{ii}^{(j)}$. Generally, the predicted values of $L_{ii}^{(j)}$ slightly increase when the mesh is coarsened (also equivalent to a reduction of $k_{\max}$). At point P_2, the grid convergence of $L_{11}^{(1)}$ is quite difficult to obtain with such a small grid size because the vicinity of the inlet boundary condition affects the longitudinal velocity on the axis $y = 0.5$ and therefore the computation of $L_{11}^{(1)}$; see Eq. (16).

Furthermore, one can remark that the third component of the mean flow is now taken into account in the model, through Eq. (11), and this might impact the decorrelation process. One can point out as well that numerical results in 3-D have been obtained from a single computation, while 10 simulations have been averaged in the 2-D validation study.

Regarding these results, one can conclude that, even if the synthesized velocity field is clearly affected by the lower spatial resolution, the present choice is a good compromise between the CPU cost and the quality of the aerodynamics modeling in the jet plume.

C. Turbulent Kinetic Energy Preservation

A snapshot of the velocity vector field in the x-y median plane is shown in Fig. 17 for a physical time $t = 20,000\Delta t$ s. The effects of the mean flow are clearly visible, in particular in the region located right after the end of the potential core where the velocity field is highly stratified. This velocity vector field is comparable to those obtained by Billson et al. [24]. One can remark that the length of the potential core prescribed by the steady RANS computation, equal to $L_c = 6.8D$, is reproduced by the stochastic simulation. In Fig. 18, a mapping of the reconstructed turbulent kinetic energy $1/2(u^2 + v^2 + w^2)$ is compared to that injected from the von Kármán–Pao spectra during the initialization of the computation, that is

$$\sum_{n=1}^{N} E(k_n)\Delta k_n$$

There are significant discrepancies between these two fields. First, a part of turbulent kinetic energy has been obviously lost during the calculation. Second, in the simulation, the energetic zone located downstream of the end of the potential core extends further

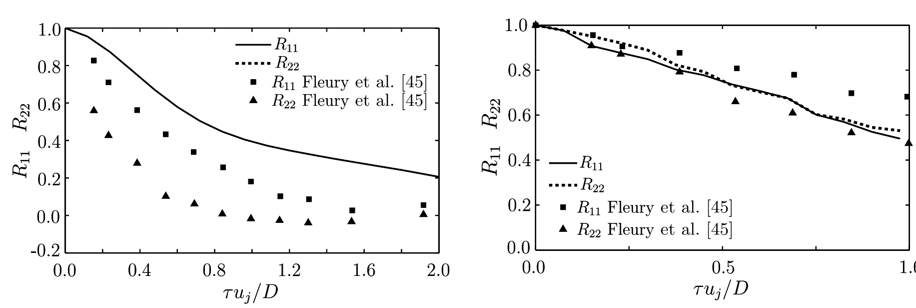

a) b)

Fig. 15 Representations of a) Eulerian decorrelation of the velocity field at the point P_2, and b) Lagrangian decorrelation of the velocity field. The reference point is P_2.

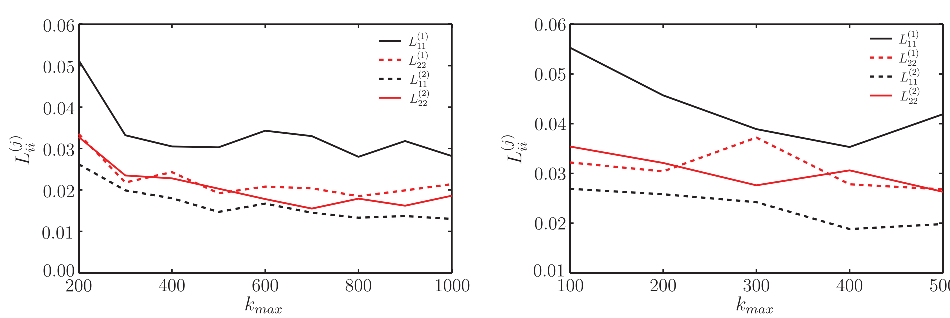

a) b)

Fig. 16 Evolution of $L_{ii}^{(j)}$ as a function of $k_{\max}$ at point a) P1, and b) P2. Results have been obtained by averaging 10 simulations with a constant $\Delta k = 5\ \mathrm{m}^{-1}$.

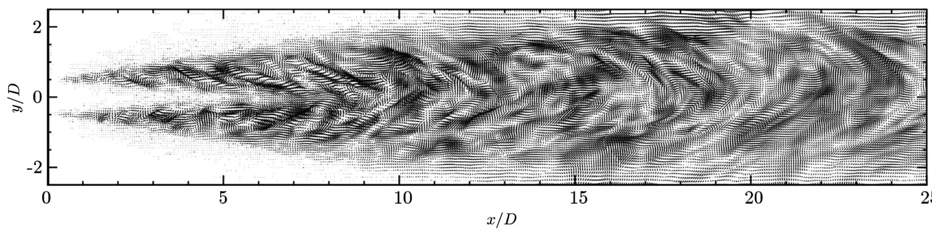

Fig. 17 Instantaneous velocity vector field

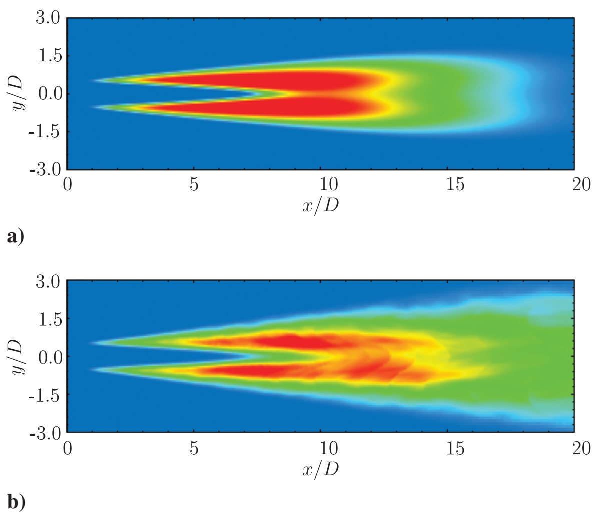

Fig. 18 k_t mapping: a) injected from the von Kármán–Pao spectra, and b) reconstructed from the stochastic field by averaging over 12,000 temporal iterations. Levels between 0 and 1000 m^2/s^2.

downstream. Nevertheless, the method is able to reproduce the two lobes located in the shear layer. This is corroborated by the turbulent kinetic energy profiles plotted in Fig. 19. The evolution of k_t along the $y = 0.5D$ axis is shown in Fig. 19a. A slight loss of energy of about 15% at $x = 8D$, where the maximum of energy is located, occurs during the calculation. Equation (11) implies that, at a given point, $\boldsymbol{u}_s$ depends on turbulence built from upstream conditions plus a certain amount of local energy. If the TKE is not a constant of space, then the injected energy cannot be exactly recovered from the stochastic velocity field.

Consequently, the loss of energy occurs during the resolution of Eq. (10) because of the inhomogeneity in k_t of the mean flow. Nevertheless, the longitudinal position corresponding to the maximum of energy is correctly modeled as well as the energy decay slope after $x = 8D$. The same conclusions can be drawn regarding Fig. 19b, which represents radial profiles of k_t at different longitudinal positions and shows that the location of the most energetic points and the energy decay at the boundary of the jet plume are both correctly mimicked. Assuming the slight loss of energy

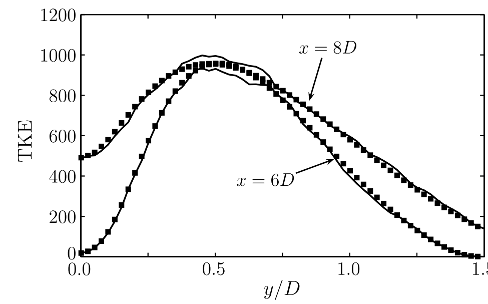

Fig. 20 Radial profiles of the turbulent kinetic energy after the energy correction.

occurring during the computation, the turbulence generation process is able to preserve the spatial distribution of the most energetic points of a given inhomogeneous mean flowfield.

D. Turbulent Kinetic Energy Correction

Because of the inhomogeneity of the mean flow, the resolution of Eq. (11) leads to turbulent kinetic energy loss. This loss is linked to the computation of the term $\boldsymbol{v}$, which carries a part of energy coming from upstream points with different flow conditions. The random field ζ is, however, built locally so that it carries the correct amount of energy. In other terms, there would be no energy loss if $\boldsymbol{u}_s$ had the same absolute value as ζ. To avoid this drawback, an adaptative correction has been tested. At each temporal iteration, the velocity field associated to small-scale structures is renormalized by applying

$$\boldsymbol{u}'_s = \frac{\|\zeta\|}{\|\boldsymbol{u}_s\|}\boldsymbol{u}_s \tag{19}$$

To do that, the 2-D computation conducted at the point P_2 in Sec. III has been repeated, considering that $\boldsymbol{u} = \boldsymbol{u}_l + \boldsymbol{u}'_s$. Radial profiles of the turbulent kinetic energy are plotted in Fig. 20. The reconstructed curve matches the initial plot. The discrepancies showing at the maximum of energy are due to the weak amount of energy contained in the cross term $\boldsymbol{u}_l \cdot \boldsymbol{u}_s$.

Regarding Fig. 21, the modeling of the decorrelation process is found to be highly damaged by the renormalization so that the temporal coherence of the velocity field is completely altered. The

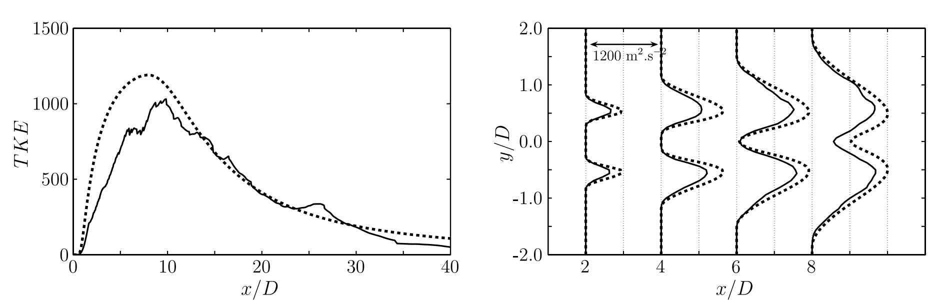

Fig. 19 Comparison between the reconstructed (solid line) and the initial TKE (dashed line): a) profile along the $y = 0.5D$ axis, and b) radial profiles at various longitudinal position x.

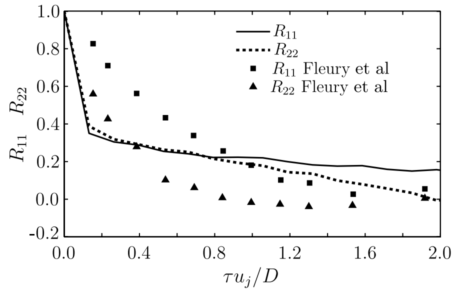

a)

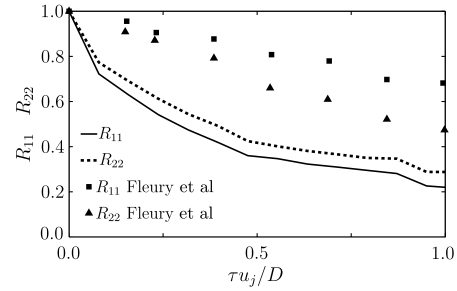

b)

Fig. 21 Representations of a) Eulerian decorrelation of the velocity field at the point P_2, and b) Lagrangian decorrelation of the velocity field. The reference point is P_2.

time and space gradients of the renormalization factor are so strong that it leads to a total decorrelation of the velocity field at large times. This solution is therefore not viable.

V. Conclusions

The sweeping-based stochastic method presented in this paper is able, starting from a given mean flowfield, to generate an unsteady turbulent velocity field that satisfies aerodynamic statistical constraints. This paper details the model validation process, achieved on a simple configuration: a free cold subsonic jet for which reference data are available. The whole 3-D subsonic jet has been modeled in only a few hours. Assuming a careful parameterization of the calibration factor α_l, the proposed approach allows the reproduction in 2-D and 3-D of the space–time velocity correlation functions and thus the correct modeling of the integral length and time scales of the flow compared to experiments. The generated turbulent field is clearly marked by the shear effect of the mean flow and takes correctly into account the advection of the turbulent structures. It allows the preservation of the spatial distribution of the most energetic points and, in the case of k_t-homogenous mean flow, ensures the conservation of turbulent kinetic energy imposed at the beginning of the computation. Furthermore, the present method has been developed to estimate acoustic sources on 3-D complex geometries such as axisymmetric isolated or nonaxisymmetric confined subsonic jets.

Owing to its ease of use, this model is also suitable for any methodology in various fields of application that requires the generation of turbulence by keeping a low computational cost. In aeroacoustics, for instance, the synthesized unsteady field can be used to compute acoustic source terms. One can notice that, in this field of application, the current model will only be able to process turbulence noise and no other mechanisms such as dipolar noise arising from von Kármán streets, for instance. As well, one can apply this methodology as Fung's kinematic simulation sweeping method to generate a homogeneous and isotropic turbulent medium for particle diffusion investigation. Then, the turbulence initialization at the inlets of direct computations could be enforced by the current model, assuming a given length of injection allowing a sufficient development of the turbulence.

Once implemented, the main difficulty of the methodology lies in the building of the mesh in accordance with the maximum wave number the user wants to model. The computational cost induced by the method is a little bit higher than the classical Stochastic Noise Generation and Radiation model because added advection equations have to be solved. However, for practical cases, this cost is lower than the one needed to solve at each time step Euler equations, for instance. Furthermore, the cost fully depends on the numerical implementation; parallel implementation using classical Message Passing Interface library could be used to reduce this cost, but it is not of our concern in the present study.

Acknowledgments

This study has been conducted in the framework of a Ph.D. thesis funded by Liebherr Aerospace Toulouse and conducted in the Computational Fluid Dynamics and Aeroacoustics Department of the ONERA in association with the École Centrale Lyon.

References

[1] Kraichnan, R., "Diffusion by a Random Velocity Field," *Physics of Fluids*, Vol. 13, No. 1, 1970, pp. 22–31. doi:10.1063/1.1692799

[2] Fung, J., Hunt, J., Malik, N., and Perkins, R., "Kinematic Simulation of Homogeneous Turbulence by Unsteady Random Fourier Modes," *Journal of Fluid Mechanics*, Vol. 236, March 1992, pp. 281–318. doi:10.1017/S0022112092001423

[3] Favier, B., Godeferd, F., and Cambon, C., "On Space and Time Correlations of Isotropic and Rotating Turbulence," *Physics of Fluids*, Vol. 22, No. 1, 2010, Paper 015101. doi:10.1063/1.3276290

[4] Thomson, D., and Devenish, B., "Particle Pair Separation in Kinematic Simulations," *Journal of Fluid Mechanics*, Vol. 526, March 2005, pp. 277–302. doi:10.1017/S0022112004002915

[5] Osborne, D., Vassilicos, J., Sung, K., and Haigh, J., "Fundamentals of Pair Diffusion in Kinematic Simulations of Turbulence," *Physical Review E*, Vol. 74, No. 3, 2006, Paper 036309. doi:10.1103/PhysRevE.74.036309

[6] Lee, S., Lele, S., and Moin, P., "Simulation of Spatially Evolving Turbulence and the Applicability of Taylor's Hypothesis in Compressible Flow," *Physics of Fluids A*, Vol. 4, No. 7, 1992, pp. 1521–1530. doi:10.1063/1.858425

[7] Klein, M., Sadiki, A., and Janicka, J., "A Digital Filter Based Generation of Inflow Data for Spatially Developing Direct Numerical or Large Eddy Simulation," *Journal of Computational Physics*, Vol. 186, No. 2, 2003, pp. 652–665. doi:10.1016/S0021-9991(03)00090-1

[8] Jarrin, N., Benhamadouche, S., Laurence, D., and Prosser, R., "A Synthetic-Eddy-Method for Generating Inflow Conditions for Large-Eddy Simulation," *International Journal of Heat and Fluid Flow*, Vol. 27, No. 4, 2006, pp. 585–593. doi:10.1016/j.ijheatfluidflow.2006.02.006

[9] Keating, A., De Prisco, G., and Piomelli, U., "Interface Conditions for Hybrid RANS/LES Calculations," *International Journal of Heat and Fluid Flow*, Vol. 27, No. 5, 2006, pp. 777–788. doi:10.1016/j.ijheatfluidflow.2006.03.007

[10] Karweit, M., Blanc-Benon, P., Juvé, D., and Comte-Bellot, G., "Simulation of the Propagation of an Acoustic Wave Through a Turbulent Velocity Field: A Study of Phase Variance," *Journal of the Acoustical Society of America*, Vol. 89, No. 1, 1991, pp. 52–62. doi:10.1121/1.400415

[11] Bechara, W., Bailly, C., Lafon, P., and Candel, S., "Stochastic Approach to Noise Modeling for Free Turbulent Flows," *AIAA Journal*, Vol. 32, No. 3, 1994, pp. 455–463. doi:10.2514/3.12008

[12] Bailly, C., and Juvé, D., "A Stochastic Approach to Compute Subsonic Noise Using Linearized Euler's Equations," *5th AIAA/CEAS Aeroacoustics Conference*, AIAA Paper 1999-1872, May 1999.

[13] Ewert, R., "Broadband Slat Noise Prediction Based on CAA and Stochastic Sound Sources from a Fast Random Particle-Mesh (RPM) Method," *Computers and Fluids*, Vol. 37, No. 4, 2008, pp. 369–387. doi:10.1016/j.compfluid.2007.02.003

[14] Billson, M., Eriksson, L., and Davidson, L., "Jet Noise Prediction Using Stochastic Turbulence Modeling," *9th AIAA/CEAS Aeroacoustics Conference*, AIAA Paper 2003-3282, May 2003.

[15] Lafitte, A., Laurendeau, E., La Garrec, T., and Bailly, C., "A Study Based on the Sweeping Hypothesis to Generate Stochastic Turbulence," *17th AIAA/CEAS Aeroacoustics Conference*, AIAA Paper 2011-2888, June 2011.

[16] Snellen, M., Van Lier, L., Golliard, J., and Védy, E., "Prediction of the Flow Induced Noise for Practical Applications Using the SNGR Method," *Proceedings of the 10th International Congress on Sound and Vibration*, Stockholm, July 2003.

[17] Omais, M., Caruelle, B., Redonnet, S., Manoha, E., and Sagaut, P., "Jet Noise Prediction Using RANS CFD Input," *5th AIAA/CEAS Aeroacoustics Conference*, AIAA Paper 2008-2938, May 2008.

[18] Dembinska, F., "Modélisation Stochastique des Sources Acoustiques Générées par la Turbulence: Application au Bruit de Jet," Ph.D. Thesis, Pierre-and-Marie-Curie Univ., Paris, 2009.

[19] Le Garrec, T., Manoha, E., and Redonnet, S., "Flow Noise Predictions Using RANS/CAA Computations," *16th AIAA/CEAS Aeroacoustics Conference*, AIAA Paper 2010-3756, June 2010.

[20] Casalino, D., and Barbarino, M., "A Stochastic Method for Airfoil Self-Noise Computation in Frequency-Domain," *16th AIAA/CEAS Aeroacoustics Conference*, AIAA Paper 2010-3884, June 2010.

[21] Bailly, C., Lafon, P., and Candel, S., "A Stochastic Approach to Compute Noise Generation and Radiation of Free Turbulent Flows," *1st AIAA/CEAS Aeroacoustics Conference*, AIAA Paper 1999-1872, June 1995.

[22] Batten, P., Goldberg, U., and Chakravarthy, S., "Reconstructed Sub-Grid Methods for Acoustic Predictions at All Reynolds Numbers," *8th AIAA/CEAS Aeroacoustics Conference*, AIAA Paper 2002-2511, June 2002.

[23] Billson, M., Eriksson, L., Davidson, L., and Jordan, P., "Modeling of Synthetic Anisotropic Turbulence and Its Sound Emission," *10th AIAA/CEAS Aeroacoustics Conference*, AIAA Paper 2004-2857, May 2004.

[24] Billson, M., Eriksson, L., and Davidson, L., "Jet Noise Modeling Using Synthetic Anisotropic Turbulence," *10th AIAA/CEAS Aeroacoustics Conference*, AIAA Paper 2004-3028, May 2004.

[25] Smirnov, A., Shi, S., and Celik, I., "Random Flow Generation Technique for Large Eddy Simulations and Particle-Dynamics Modeling," *Journal of Fluids Engineering*, Vol. 123, No. 2, 2001, pp. 359–371. doi:10.1115/1.1369598

[26] Fung, J., and Vassilicos, J., "Kinematics Simulation of Homogeneous Turbulence by Unsteady Random Fourier Modes," *Physical Review E*, Vol. 57, No. 2, 1998, p. 1677. doi:10.1103/PhysRevE.57.1677

[27] Chicheportiche, J., "Calcul Direct du Rayonnement Acoustique Généré par une Cavité Cylindrique Sous une Aile d'Avion," Ph.D. Thesis, Arts et Métiers ParisTech, Paris, 2011.

[28] Na, Y., and Moin, P., "Direct Numerical Simulation of a Separated Turbulent Boundary Layer," *Journal of Fluid Mechanics*, Vol. 374, Nov. 1998, pp. 379–405. doi:10.1017/S0022112098009987

[29] Careta, A., Sagués, F., and Sancho, J., "Stochastic Generation of Homogenous Isotropic Turbulence with Well-Defined Spectra," *Physical Review E*, Vol. 48, No. 3, 1993, pp. 2279–2287. doi:10.1103/PhysRevE.48.2279

[30] Ewert, R., and Edmunds, R., "CAA Slat Noise Studies Applying Stochastic sound Sources Based on Solenoidal Filters," *11th AIAA/CEAS Aeroacoustics Conference*, AIAA Paper 2005-2862, May 2005.

[31] Ewert, R., Dierke, J., Pott-Pollenske, M., Appel, C., Edmunds, R., and Sutcliffe, M., "CAA-RPM Prediction and Validation of Slat Setting Influence on Broadband High-Lift Noise Generation," *16th AIAA/CEAS Aeroacoustics Conference*, AIAA Paper 2010-3883, June 2010.

[32] Siefert, M., and Ewert, R., "Sweeping Sound Generation in Jets Realized with a Random Particle-Mesh Method," *15th AIAA/CEAS Aeroacoustics Conference*, AIAA Paper 2009-3369, May 2009.

[33] Ewert, R., Dierke, J., Siebert, J., Neifeld, A., Appel, C., Siefert, M., and Kornow, O., "CAA Broadband Noise Prediction for Aeroacoustic Design," *Journal of Sound and Vibration*, Vol. 330, No. 17, 2011, pp. 4139–4160. doi:10.1016/j.jsv.2011.04.014

[34] Dieste, M., and Gabard, G., "Broadband Fan Interaction Noise Using Synthetic Inhomogeneous Non-Stationary Turbulence," *17th AIAA/CEAS Aeroacoustics Conference*, AIAA Paper 2011-2708, June 2011.

[35] Dieste, M., and Gabard, G., "Random Particle Methods Applied to Broadband Fan Interaction Noise," *Journal of Computational Physics*, Vol. 231, No. 24, 2012, pp. 8133–8151. doi:10.1016/j.jcp.2012.07.044

[36] Dieste, M., and Gabard, G., "Synthetic Turbulence Applied to Broadband Interaction Noise," *15th AIAA/CEAS Aeroacoustics Conference*, AIAA Paper 2009-3267, May 2009.

[37] Dieste, M., and Gabard, G., "Random-Vortex-Particle Methods for Broadband Fan Interaction Noise," *16th AIAA/CEAS Aeroacoustics Conference*, AIAA Paper 2010-3885, June 2010.

[38] Neifeld, A., and Ewert, R., "Jet Mixing Noise from Single Stream Jets Using Stochastic Source Modeling," *17th AIAA/CEAS Aeroacoustics Conference*, AIAA Paper 2011-2700, June 2011.

[39] Ewert, R., Neifeld, A., and Fritzsch, A., "A 3-D Modal Stochastic Jet Noise Source Model," *17th AIAA/CEAS Aeroacoustics Conference*, AIAA Paper 2011-2887, June 2011.

[40] Jarrin, N., Prosser, R., Uribe, J., Benhamadouche, S., and Laurence, D., "Reconstruction of Turbulent Fluctuations for Hybrid RANS/LES Simulations Using a Synthetic-Eddy Method," *International Journal of Heat and Fluid Flow*, Vol. 30, No. 3, 2009, pp. 435–442. doi:10.1016/j.ijheatfluidflow.2009.02.016

[41] Chen, S., and Kraichnan, R., "Sweeping Decorrelation in Isotropic Turbulence," *Physics of Fluids A*, Vol. 1, No. 12, 1989, pp. 2019–2025. doi:10.1063/1.857475

[42] Nelkin, M., and Tabor, M., "Time Correlations and Random Sweeping in Isotropic Turbulence," *Physics of Fluids A*, Vol. 2, No. 1, 1990, pp. 81–83. doi:10.1063/1.857684

[43] Praskovsky, A., Gledzer, E., Kuryakin, M., and Zhou, Y., "The Sweeping Decorrelation Hypothesis and Energy-Inertial Scale Interaction in High Reynolds Number Flows," *Journal of Fluid Mechanics*, Vol. 248, March 1993, pp. 493–511. doi:10.1017/S0022112093000862

[44] Bailly, C., Gloerfelt, X., and Bogey, C., "Report on Stochastic Noise Source Modelling," École Centrale de Lyon, Tech. Rept. UMR-CNRS-5509, JEAN Projet, 2002.

[45] Fleury, V., Bailly, C., Jondeau, E., Michard, M., and Juvé, D., "Space–Time Correlations in Two Subsonic Jets Using Dual Particle Image Velocimetry Measurements," *AIAA Journal*, Vol. 46, No. 10, 2008, pp. 2498–2509. doi:10.2514/1.35561

[46] Gloerfelt, X., Bailly, C., and Bogey, C., "Full 3-D Application of the SNGR Method to Isothermal Mach 0.9 jet (Jet 4)," École Centrale de Lyon, Final Rept. UMR-CNRS-5509, JEAN Projet, 2003.

[47] Muller, F., "Simulation de Jets Propulsifs: Application à l'Identification de Phénomènes Générateurs de Bruit," Ph.D. Thesis, Numerical Simulation and Aeroacoustic Dept., ONERA–The French Aerospace Lab., Châtillon, France, 2006.

[48] Lafitte, A., Laurendeau, E., Le Garrec, T., and Bailly, C., "Prediction of Subsonic Jet Noise Relying on a Sweeping Based Turbulence Generation Process," *18th AIAA/CEAS Aeroacoustics Conference*, AIAA Paper 2012-2149, June 2012

[49] Lafitte, A., Laurendeau, E., Le Garrec, T., and Bailly, C., "Jet Noise Prediction Using a Sweeping Based Turbulence Generation Process," *Acoustics 2012, 11ème Congrès Français d'Acoustique and 2012 Annual IOA*, Inst. of Acoustics, Nantes, France, April 2012, pp. 1317–1322.

[50] Bogey, C., and Bailly, C., "A Family of Low Dispersive and Low Dissipative Explicit Schemes and Noise Computations," *Journal of Computational Physics*, Vol. 194, No. 1, 2004, pp. 194–214. doi:10.1016/j.jcp.2003.09.003

[51] Tam, C. K. W., and Dong, Z., "Radiation and Outflow Boundary Conditions for Direct Computation of Acoustic and Flow Disturbances in a Nonuniform Mean Flow," *Journal of Computational Acoustics*, Vol. 4, No. 2, 1996, pp. 175–201. doi:10.1142/S0218396X96000040

A. Lyrintzis
Associate Editor